

Rapid Combined T_1 and T_2 Mapping Using Gradient Recalled Acquisition in the Steady State

Sean C.L. Deoni,^{1,2} Brian K. Rutt,^{1–3} and Terry M. Peters^{1–3*}

A novel, fully 3D, high-resolution T_1 and T_2 relaxation time mapping method is presented. The method is based on steady-state imaging with T_1 and T_2 information derived from either spoiling or fully refocusing the transverse magnetization following each excitation pulse. T_1 is extracted from a pair of spoiled gradient recalled echo (SPGR) images acquired at optimized flip angles. This T_1 information is combined with two refocused steady-state free precession (SSFP) images to determine T_2 . T_1 and T_2 accuracy was evaluated against inversion recovery (IR) and spin-echo (SE) results, respectively. Error within the T_1 and T_2 maps, determined from both phantom and in vivo measurements, is approximately 7% for T_1 between 300 and 2000 ms and 7% for T_2 between 30 and 150 ms. The efficiency of the method, defined as the signal-to-noise ratio (SNR) of the final map per voxel volume per square root scan time, was evaluated against alternative mapping methods. With an efficiency of three times that of multipoint IR and three times that of multi-echo SE, our combined approach represents the most efficient of those examined. Acquisition time for a whole brain T_1 map ($25 \times 25 \times 10$ cm) is less than 8 min with 1 mm^3 isotropic voxels. An additional 7 min is required for an identically sized T_2 map and postprocessing time is less than 1 min on a 1 GHz PIII PC. The method therefore permits real-time clinical acquisition and display of whole brain T_1 and T_2 maps for the first time. *Magn Reson Med* 49:515–526, 2003. © 2003 Wiley-Liss, Inc.

Key words: T_1 ; T_2 ; SSFP; SPGR; relaxation time mapping; rapid volumetric imaging

A fast and accurate method of determining the longitudinal, T_1 , and transverse, T_2 , relaxation constants on a voxel-by-voxel basis has long been a goal of MRI scientists. Rigorous characterization of T_1 and T_2 may allow for greater tissue discrimination, segmentation, and classification, thereby improving disease detection and monitoring, as well as enhancing the images used for image-guided surgical procedures. Absolute determination of T_1 and T_2 is clinically useful in areas such as in-flow perfusion studies (1) and dynamic contrast agent studies (2), as well as in the diagnosis of epilepsy (3) and in determining the severity of Parkinson's disease (4). Therefore, a method that

permits simultaneous T_1 and T_2 determination in a rapid manner would be useful in a wide range of imaging applications.

In order to be clinically useful for neuroimaging applications, T_1 and T_2 maps should be of high resolution, with a voxel volume less than 1 mm^3 , and have low noise. Imaging time should be less than 30 min for a large volume ($25 \times 25 \times 10$ cm) with minimal postprocessing time. Ideally, postprocessing would be performed at the scanner console.

Despite the long acquisition times, the principal methods for T_1 and T_2 mapping remain inversion-recovery (IR) and saturation-recovery (SR) for T_1 , and spin echo (SE) and multiple or fast spin echo (mSE, FSE) for T_2 . Although alternative methods (5–9) have been developed to rapidly and accurately determine T_1 or T_2 , the low signal-to-noise ratio (SNR), lengthy reconstruction time, or special hardware requirements associated with these newer methods reduce their appeal.

The variable nutation angle method originally introduced in 1974 (10) and investigated by a number of authors (11–14) calculates T_1 with an accuracy similar to that achieved by the IR and SR techniques, but with a significant decrease in acquisition time. The sequence involves establishing a spoiled steady state followed by the collection of spoiled gradient echo (SPGR) images over a range of flip angles. This generates a signal curve that depends on T_1 and which is easily linearized, allowing for quick T_1 determination. We believe that this method is the most appropriate for use in 3D T_1 mapping due to the rapid acquisition, high measurement precision, and efficient postprocessing.

First described some 40 years ago (15), the steady-state free precession (SSFP) pulse sequence has received attention recently as a high-speed, highly efficient imaging method. The underlying sequence is similar to SPGR, but differs in one respect: both longitudinal *and* transverse magnetization are brought into dynamic equilibrium through the application of α pulses and fully refocusing the transverse magnetization prior to each excitation pulse. Collecting SSFP images over a range of flip angles yields a signal curve that is a function of both T_1 and T_2 (16). We demonstrate in this article that this signal curve can also be cast into a linear form, allowing for rapid determination of T_2 , provided T_1 is known. Thus, performing variable nutation angle SPGR and SSFP experiments sequentially allows us to determine both T_1 and T_2 relaxation times significantly faster than is possible with existing methods.

In this article we introduce the use of variable nutation SPGR and SSFP for combined T_1 and T_2 quantification and examine the parameters of SPGR and SSFP that influence the precision of the T_1 and T_2 estimates. Specifically, we

¹Imaging Research Laboratories, Robarts Research Institute, London, Ontario, Canada.

²Department of Medical Biophysics, University of Western Ontario, London, Ontario, Canada.

³Department of Diagnostic Radiology and Nuclear Medicine, University of Western Ontario, London, Ontario, Canada.

Grant sponsor: Canadian Institutes for Health Research; Grant numbers: MT-11540; GR-14973; Grant sponsors: University of Western Ontario; General Electric Medical Systems.

*Correspondence to: Terry M. Peters, Imaging Research Laboratories, Robarts Research Institute, P.O. Box 5015, 100 Perth Drive, London, Ontario N6A 5K8, Canada. E-mail: tpeters@imaging.robarts.ca

Received 19 February 2002; revised 16 October 2002; accepted 20 October 2002.

DOI 10.1002/mrm.10407

Published online in Wiley InterScience (www.interscience.wiley.com).

© 2003 Wiley-Liss, Inc.

examine the role of repetition time and the optimization of the flip angles for high-speed mapping. Following these optimizations, we show how the method, using SPGR and SSFP data acquired from just two flip angles each, can be used for rapid 3D volumetric T_1 and T_2 mapping of the brain. Finally, we characterize the efficiency of our optimized method by comparing it with existing conventional and accelerated methods. Based on a metric of SNR efficiency in the final T_1 and T_2 maps, we show that the proposed method is superior to the traditional approaches and allows fully 3D combined T_1 and T_2 mapping to be achieved in a clinically acceptable scanning time. We have extended the naming convention originally used in (11) to refer to our optimized variable nutation SPGR and SSFP; we call the former approach DESPOT1 and the latter DESPOT2, reflecting the T_1 and T_2 mapping properties of these techniques.

THEORY

Basic DESPOT1 Theory

A thorough theoretical description of SPGR has been given previously (5), so we simply state that the measured SPGR signal intensity (S_{SPGR}) is a function of the longitudinal relaxation time, T_1 , repetition time, TR , flip angle, α , and a factor which is proportional to the equilibrium longitudinal magnetization, M_o :

$$S_{SPGR} = \frac{M_o(1 - E_1)\sin(\alpha)}{1 - E_1\cos(\alpha)} \quad [1]$$

where $E_1 = \exp(-TR/T_1)$.

By holding TR constant and incrementally increasing α , a curve characterized by T_1 is generated. As demonstrated in Ref. 5, these data can be represented in the linear form, $Y = mX + b$ as:

$$\frac{S_{SPGR}}{\sin(\alpha)} = E_1 \frac{S_{SPGR}}{\tan(\alpha)} + M_o(1 - E_1) \quad [2]$$

from which the slope, m , and the Y-intercept, b , can be estimated by linear regression, allowing T_1 and M_o to be extracted:

$$T_1 = -TR/\ln(m) \quad [3a]$$

$$M_o = b/(1 - m). \quad [3b]$$

Basic DESPOT2 Theory

The general SSFP sequence involves the repeated application of excitation pulses with flip angle α at a TR much less than either T_1 or T_2 . With perfect refocusing of the spins, a steady state is achieved in both the longitudinal and transverse magnetizations. The signal intensity (S_{SSFP}) is therefore expressed as a function of the tissue T_1 and T_2 relaxation times, TR , α , and M_o . However, the literature contains multiple forms of the SSFP signal equation (15,17–21). In our case, where TR is kept short (less than 10 ms) and the RF pulses are alternated by 180° , the

equation derived by Perkins and Wehrli (18) is the most appropriate:

$$S_{SSFP} = \frac{M_o(1 - E_1)\sin(\alpha)}{1 - E_1E_2 - (E_1 - E_2)\cos(\alpha)} \quad [4]$$

where $E_2 = \exp(-TR/T_2)$.

Holding TR constant and incrementally increasing α generates data that depend on both T_1 and T_2 . Equation [4] can be recast into the linear form $Y = mX + b$, giving us:

$$\frac{S_{SSFP}}{\sin(\alpha)} = \frac{E_1 - E_2}{1 - E_1E_2} \times \frac{S_{SSFP}}{\tan(\alpha)} + \frac{M_o(1 - E_1)}{1 - E_1E_2}. \quad [5]$$

If T_1 (and hence E_1) is known, T_2 and M_o can be calculated from the values of slope (m) and intercept (b) as:

$$T_2 = -TR/\ln\left(\frac{m - E_1}{mE_1 - 1}\right) \quad [6a]$$

$$M_o = b(E_1E_2 - 1)/(1 - E_1). \quad [6b]$$

Optimum DESPOT1 Flip Angles: Numerical Solution

Previous authors (12,13), and most notably Wang et al. (14), have investigated the parameters that influence the variable nutation SGPR T_1 estimate precision. In their approach they begin with a set of standard flip angles (SA) = {10,20,30...80,90,100°} and examine the effect of altering TR for a given T_1 . Using this approach, Wang et al. reported that optimum T_1 precision occurs when the TR/T_1 ratio is approximately 1.1:1. They also showed that the precision obtained using 10 flip angles can be achieved using just two optimized angles with a corresponding 5-fold reduction in imaging time. The two optimized angles were determined via an iterative method, which minimized the T_1 estimate variance. Unfortunately, their method does not reveal the mechanism that determines T_1 precision. As a result, they do not provide a simple one-step method for determining the two angles.

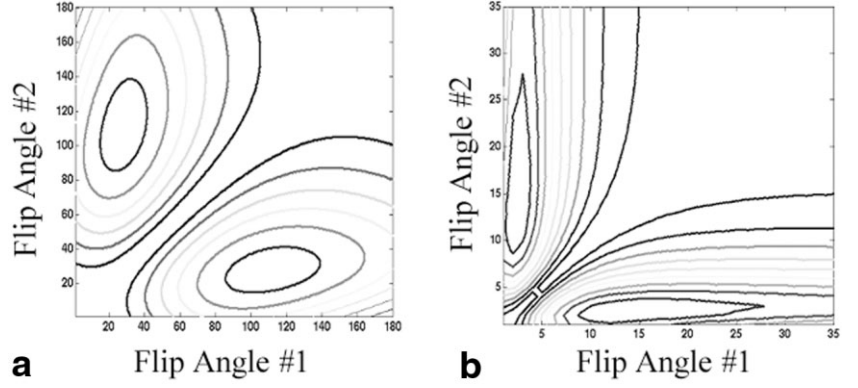
To determine which two angles to use for a particular TR/T_1 combination in a more straightforward manner, consider the estimation of T_1 from the linearized signal. The two signal intensities provide two points on the regression line. If each point suffers the same uncertainty, the further the two points are separated along the line, the better the estimate of slope. This separation along the ordinate can be defined as the normalized dynamic range (DR) of the regression line, given by:

$$DR = \frac{S\alpha_2}{M_o\sin(\alpha_2)} - \frac{S\alpha_1}{M_o\sin(\alpha_1)} \quad [7]$$

where α_1 and α_2 are the two flip angles and $S\alpha_1$ and $S\alpha_2$ are the SPGR signals associated with α_1 and α_2 .

In our case, the data points do not suffer the same uncertainty; rather, the precision depends on the location of the points along the line and generally decreases as the two points move away from the midpoint (defined by the location of the peak of the signal curve and given by the

FIG. 1. Contour plots of the dynamic range \times fractional signal as a function of α_1 and α_2 for **a**: $TR = 800$ ms and $T_1 = 1000$ ms; the optimum angles are 29° and 112° . **b**: $TR = 5$ ms and $T_1 = 1000$ ms; the optimum angles are 3° and 13° . Contours span the range [6, 73] in **a** and [3, 46] in **b**.



Ernst signal ($S\alpha_E$). This means that the precision can be related to the fractional signal of the points (FS).

$$FS = (S\alpha_1 + S\alpha_2)/2S\alpha_E. \quad [8]$$

With the above considerations of the trade-off between DR and FS , we propose that optimum T_1 precision will be achieved when the product of $DR \times FS$ is maximized.

Figure 1a is a resultant plot of $DR \times FS$, from which the ideal angles can be determined. In this example, where we have used the same values as Wang et al. ($TR = 800$ ms, $T_1 = 1000$ ms), we confirm their prediction of the ideal angles as 29° and 112° . Due to the strong agreement between our results and those of Wang et al., we believe the $DR \times FS$ product can be used to determine the ideal angles for any TR/T_1 case.

In our application we are interested in using very low TR values, i.e., <5 ms. Results of an analysis similar to the above with $TR = 5$ ms and $T_1 = 1000$ ms are presented in Fig. 1b. In this case, the ideal angles are shown to be 3° and 13° , which are quite different from those found in the high TR case. The impact of angle choice is clearly demonstrated in these two examples and stresses the need for a simple method of determining the ideal angles for arbitrary TR/T_1 combinations.

Optimum DESPOT1 Flip Angles: Analytical Solution

While we have shown that it is possible to determine the two ideal angles by searching for maxima in the $DR \times FS$ space, the process is time-consuming and so fails to pro-

vide a simple analytical method of determining the ideal angles for arbitrary TR/T_1 combinations.

Derivation of an analytical prediction of optimal dual SPGR angles requires the following simplifications. By plotting the $DR \times FS$ product over a wide search-space, it becomes apparent that this product is maximized when $S\alpha_1 = S\alpha_2$. Therefore, we simplify FS to f :

$$f = S\alpha_1/S\alpha_E = S\alpha_2/S\alpha_E. \quad [9]$$

In Fig. 2a, this new function ($DR \times f$) is plotted against TR/T_1 and f . Fitting a polynomial for each TR/T_1 case and solving for the maximum, we find that over the complete range of TR/T_1 investigated the function is maximized at $f = 0.71$. Therefore, T_1 precision is maximized by choosing the flip angles such that $S\alpha_1 = S\alpha_2 = 0.71S\alpha_E$.

We can now derive a general analytical solution for the two ideal angles. Expanding $S = f \times S\alpha_E$ using Eq. [1] we obtain:

$$\frac{\sin(\alpha)}{1 - E_1 \cos(\alpha)} = \frac{f \times \sin(\alpha_E)}{1 - E_1 \cos(\alpha_E)}. \quad [10]$$

Following the derivation shown in Appendix A, we obtain a solution for the angles as:

$$\alpha = \cos^{-1} \left(\frac{f^2 E_1 \pm (1 - E_1^2) \sqrt{1 - f^2}}{1 - E_1^2 (1 - f^2)} \right). \quad [11]$$

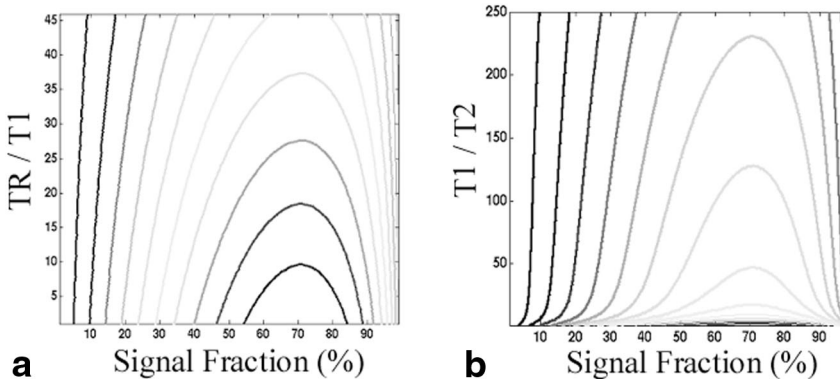


FIG. 2. **a**: $DR \times f$ calculated over the search-space $0 < S_{\alpha_{1,2}}/S\alpha_E < 100\%$ and $0 < TR/T_1 < 50$. Maximum precision occurs when $S_{\alpha_{1,2}}/S\alpha_E = 0.71$. **b**: $DR \times f$ calculated over the search-space $0 < S_{\alpha_{1,2}}/S\alpha_E < 100\%$ and $0 < T_1/T_2 < 250$. T_2 precision is maximum when $S_{\alpha_{1,2}}/S\alpha_E = 0.71$. Curves represent $DR \times f$ over the range [5, 76] in **a** and [5, 51] in **b**.

Although more complex, Eq. [15] is of the same form as the Ernst angle formula, to which it reduces when $f = 1.0$.

Optimum DESPOT2 Flip Angles

Following an analysis similar to that presented in the previous sections, we can determine the angles that maximize the precision in the T_2 estimate for a specific TR , T_1 , and T_2 set. Evaluating $DR \times FS$ (where DR is as defined in Eq. [7] with the modification that S is now the signal associated with the SSFP sequence) over the four-dimensional search-space defined by TR/T_1 , TR/T_2 , S_{α_1} , and S_{α_2} we have found that TR/T_1 and TR/T_2 can be combined into the single variable T_1/T_2 without loss of generality. Examining $DR \times FS$ in this new 3D search-space reveals that this product is once again maximized when $S_{\alpha_1} = S_{\alpha_2}$. Therefore, we simplify FS to f .

In Fig. 2b, $DR \times f$ is plotted against T_1/T_2 and f . Once again, fitting a polynomial for each case and solving for the maximum, we find that over the range of T_1/T_2 investigated (0–250), the maximum occurs at $f = 0.71$. We conclude that maximum T_2 precision is achieved by choosing the flip angles such that $S_{\alpha_1} = S_{\alpha_2} = 0.71S_{\alpha_E}$.

Using this result and the same algebraic steps as presented for the SPGR case, the following analytical expression for the two ideal SSFP angles is derived (full derivation shown in Appendix B):

$$\alpha = \cos^{-1}((-B \pm \sqrt{B^2 - 4AC})/2A) \quad [12]$$

where A , B , and C are as derived in Appendix B and the angles are the two roots of Eq. [12].

Optimum Experiment Design

In addition to determining the flip angles that yield maximum T_1NR and T_2NR , it is also useful to determine how to best allocate a specified exam time so as to maximize the combined precision of T_1 and T_2 . This is achieved by maximizing the variable $(T_1NR + T_2NR)$. Following the laws for propagation of error, as outlined in Appendix C, we obtain the following expression for $(T_1NR + T_2NR)$:

$$T_1NR + T_2NR = SNR_{SPGR} \times G_1 + SNR_{SSFP} \times G_2 \quad [13]$$

where G_1 and G_2 are as defined in the appendix. We can rewrite Eq. [13] in terms of experiment time as:

$$T_1NR + T_2NR = (TG_1/Ta) + TG_2/(To - Ta) \quad [14]$$

where To is the total exam time, $T = 0.5To$, and Ta is time spent collecting DESPOT1 data.

Differentiating Eq. [14] shows that $(T_1NR + T_2NR)$ is maximized when:

$$Ta = 0.5 \times (2G_1 \pm 2\sqrt{G_1G_2To})/(G_1 - G_2). \quad [15]$$

For most clinical anatomical imaging applications ($T_1 = 100\text{--}3000$ ms, $T_2 = 30\text{--}600$ ms, $TR = 5$ ms), evaluation of Eq. [15] shows T_1 and T_2 precision is generally maximized

when 75% of the exam time is devoted to collecting T_1 data.

Comparisons With Existing Methods

In addition to optimizing the precision of the DESPOT1 and DESPOT2 approaches, we compare our method with alternative mapping strategies to determine the relative merit of our technique. A system for theoretically comparing various T_1 mapping methods has been presented by Crawley and Henkelman (22) and is based on a measure of precision per unit scan time. To experimentally compare the sequences, we modified the Crawley and Henkelman metric to:

$$\Lambda = \frac{T_1NR}{V\sqrt{T_{seq}}}, \quad [16]$$

where V is the voxel volume and T_1NR is the experimentally derived parameter defined previously. Normalization with respect to voxel volume and square root of scan time (T_{seq}) allows fair comparison between published and experimental data.

For the T_2 maps, the same comparison metric was used with T_2NR replacing T_1NR .

METHODS

Both numerical simulations and experiments were designed to assess the DESPOT1 and DESPOT2 T_1 and T_2 precision. Numerical simulations consisted of 65,000 T_1 or T_2 estimations in which the calculated signal intensity values were superimposed on Gaussian distributed random noise (zero mean, 0.01 M_0 standard deviation). Experimental data were collected from both phantoms and human volunteers. Ethics approval for the human studies was obtained from the Ethics Review Board Committee of the University of Western Ontario.

Simulation Methods

Preceding sections dealt with maximizing the T_1 and T_2 measurement precision using just two flip angles. In the case of SPGR, Wang et al. (14) showed that T_1 calculated from two ideally chosen angles has the same precision as T_1 determined from 10 uniformly spaced angles. Although they optimized the pair of flip angles in their experiment, they did not optimize the 10 angles. We believe this did not provide a fair comparison between the two cases; in addition, Wang's argument may not hold for all values of TR/T_1 .

Examining the behavior of the SPGR signal curve, we note that as TR is decreased for a given T_1 , the peak of the signal curve decreases and shifts to the left. Sampling for $TR/T_1 = 1.1$ using set SA produces points symmetrically disposed about the peaked region of the curve. Using these same angles for $TR/T_1 = 0.01$, only one side of the peak is sampled. When the peaked region of the signal curve is sampled symmetrically, the points along the regression line are uniformly distributed. Oversampling either side of the peak results in clustered points at either end of the regression line.

We propose that for optimal T_1 precision, the flip angles must symmetrically sample the signal curve. This is achieved by enforcing uniform sampling along the regression line. We refer to angles meeting this requirement as “tuned angles.” If this condition is met, we believe the precision in T_1 using 10 tuned angles will be greater than the two ideal angles for all values of T_1 .

Numerical simulations were performed to confirm this hypothesis. The T_1NR was evaluated for a range of T_1 values (300–2000 ms) with a single TR (5 ms) using data from the standard set of 10 angles; the set of 10 tuned angles; and the two ideal angles (calculated using Eq. [11]), as well as from the two ideal angles averaged five times. We refer to this analysis as numerical simulation 1.

In a clinical setting the length of time available for an MR exam is limited and it is therefore important to use that time as effectively as possible. Thus, we must consider a time constraint when optimizing MR parameters. In our application, we can maximize the precision in the T_1 or T_2 measurement either by increasing the number of flip angles (N_{fa}) acquired, or averaging (N_{av}) several acquisitions of a smaller set of angles. To determine which of these options produces the greatest precision within the same scan time, the T_1NR and T_2NR were calculated from 2 through 100 tuned flip angles without averaging and from the two ideal angles averaged 1 through 50 times. Additionally, the combined effect of averaging and sampling was examined. Using a scan time limit that allowed a total of 100 angles to be sampled, we calculated T_1NR and T_2NR for the eight even combinations; 2 angles averaged 50 times, 4 averaged 25 times, etc. (numerical simulation 2).

We also investigated the variation in the precision of SSFP by evaluating T_2NR over an $8 \times 16 T_2 \times T_1$ grid (T_2 : 30–100 ms and T_1 : 300–2000 ms). Additionally, we investigated the sensitivity of the T_2 measurements to T_1 imprecision by calculating T_2NR over the same $T_2 \times T_1$ grid with T_1 values randomly chosen from a probability distribution characterized by a Gaussian relationship with a standard deviation equal to 10% of the nominal T_1 (numerical simulation 3).

Experimental Methods

Building on the numerical simulations, we performed a series of experiments using both phantoms and human data. The phantoms consisted of two cylindrical holders, each containing eight agarose gel tubes doped with nickel chloride providing (in total) a $4 \times 4 T_1 \times T_2$ grid with T_1 values \approx 250, 500, 1000, and 2000 ms, and T_2 values \approx 30, 50, 100, and 130 ms.

Throughout the next sections, a number of imaging sequences are used repeatedly. In the interest of space, we list the general parameters here.

IR: $TE = 15$ ms, $TR = 5000$ ms, $TI = (50, 100, 200, 400, 800, 1600, 3200)$ ms.

FSE-IR: same as IR with an echo train length (ETL) of 4.

SR: $TE = 15$ ms, $TR = (250, 500, 750, 1000, 1500, 2000, 4000, 6000)$ ms.

SE: $TE = (20, 40, 80, 160, 320, 640, 1320)$ ms, $TR = 5000$ ms.

FSE: $TE = (20, 40, 60, 80, 100, 150, 195)$ ms, $TR = 5000$ ms, $ETL = 12$.

Matrix size in all cases was $128 \times 256 \times 1$ with a 5 mm slice thickness, 25 cm FOV, and ± 61.25 kHz bandwidth. DESPOT1: $TE = 1.1$ ms, $TR = 3.4$ ms, flip angles = (3° and 12°).

DESPOT2: $TE = 1.6$ ms, $TR = 3.4$ ms, flip angles = (20° and 80°).

For DESPOT1 and DESPOT2, matrix size was $256 \times 256 \times 24$ with a 1 mm slice thickness, 25 cm FOV, and ± 31.25 kHz bandwidth.

Reference T_1 values throughout the phantom and the brain of a single healthy 21-year-old male volunteer (at the level of the lateral ventricles) were determined using a single-slice IR sequence. Total imaging time was 75 min for each set of data. T_1 values were calculated using a three-parameter nonlinear least squares fitting routine to solve the equation: $S(TI) = S_o(1 - \rho \exp(-TI/T_1))$ for S_o , ρ , and T_1 , with ρ included to account for imperfect inversion pulses.

Phantom and brain T_2 values were determined using a clinical single-slice SE sequence. Imaging time was 75 min for each experiment. T_2 values were determined voxel-wise using a two-parameter nonlinear least squares fitting routine to solve the equation: $S(TE) = M_o \exp(-TE/T_2)$ for M_o and T_2 .

From the resultant maps we calculated regional T_1 and T_2 values for six common tissues: frontal gray matter (GM), frontal white matter (WM), globus pallidus (GP), caudate nucleus (CN), thalamus (T), and putamen (P).

We also calculated phantom and brain T_1 and T_2 values from 3D DESPOT1 and DESPOT2 averaged five times. Total combined imaging time was 20 min.

We outlined above a set of criteria for achieving clinically practical T_1 and T_2 mapping. To confirm that an imaging sequence that combines DESPOT1 and DESPOT2 meets these criteria, whole-brain DESPOT1 and DESPOT2 data were collected from a healthy 22-year-old female volunteer using a $256 \times 256 \times 100$ matrix over a $25 \text{ cm}^2 \times 10$ cm volume with SPGR parameters: flip angles = (3° , 12°), $TR = 3.6$ ms, $TE = 1.6$ ms, ± 62.5 kHz BW, and $NEX = 2$; SSFP parameters: flip angles = (20° , 80°), $TR = 4.1$ ms, $TE = 1.2$ ms, ± 125 kHz BW, and $NEX = 2$. Combined imaging time for the two sequences was 13 min.

To validate the error propagation theory and the prediction that maximum $T_1NR + T_2NR$ is achieved when 75% of the exam time is spent collecting the T_1 data, we performed the following experiment using the agarose phantoms. With an image limit of 20, the exam time was divided in the following $T_1:T_2$ manner: 18:2, 16:4, 14:6, 12:8, 10:10, 8:12, 6:14, 4:16, and 2:18. We then calculated the $T_1NR + T_2NR$ sum for each of these combinations. Imaging parameters were the same as in the previous phantom experiments.

Finally, we determined the reproducibility (average percentage SD of repeated the T_1 and T_2 measurements) of the method by collecting phantom DESPOT1 and DESPOT2 data on four separate occasions. Imaging parameters were the same as outlined in the previous phantom experiments using the two ideal angles. The number of averages for

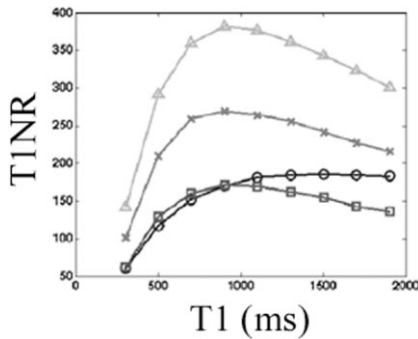


FIG. 3. Simulated T_1NR values calculated over a range of T_1 values calculated from data acquired with the standard set of angles (circle), tuned angles (star), ideal angles (square), and the ideal angles average 5 times (triangle). Maximum precision is achieved through averaging the ideal angle data.

both experiments was increased to bring the total scan time to 13 min, the same time required for the whole brain maps.

Comparison Methods

Experimental T_1NR measurements were calculated from single-slice, 8-point IR, SR, and FSE-IR acquisitions as well as 3D DESPOT1 acquisitions from the brains of five healthy volunteers ranging in age from 20–24. Slices were axially oriented at the level of the lateral ventricles (256×128 matrix zero-padded to 256×256 , 25 cm² FOV and 5 mm ST).

Additional comparisons were made with three widely used accelerated T_1 mapping techniques: SNAPSHOT-FLASH (5), Look-Locker (6), and accelerated 3D Look-Locker (7). Unfortunately, we did not have access to the pulse sequence codes for these methods and thus the comparison was based on literature values derived from the respective articles. For this reason, analysis was restricted to WM and GM only.

Experimental T_2NR measurements were also calculated from single slice, 7-point SE and FSE acquisitions as well

as from 3D DESPOT2 data. T_2 measurements were also derived from 2-point SE and FSE data using the lowest and highest TE values collected in the SE and FSE experiments.

We also compared our T_2 results with those produced by T_2 FARM (8) and SNAPSHOT-FLASH (9). Since we did not have access to either of these pulse sequence codes, we were limited to using values quoted by the authors of those sequences.

RESULTS

Simulation Results

The advantage of tuning the flip angles for the T_1 range of interest is clearly demonstrated in the results of the first set of simulations (Fig. 3). On average, using the tuned set of angles increases the T_1NR by a factor of 1.5 compared to the standard uniformly spaced angle set. Unlike the results reported in Ref. 14, which showed a decrease in precision in the 10-angle case compared to the 2-angle case, our results show the average T_1NR is increased by a factor of 1.6 using the 10 tuned angles over the 2 ideal angles when the 10 angles are appropriately chosen. However, with the exam time held constant (by averaging the ideal dual-angle data five times), the T_1NR of the dual-angle T_1 maps exceeds that of the standard and tuned angle T_1 maps by factors of 2 and 1.4, respectively. This result suggests that multiple averaging of dual-angle T_1 maps is the most efficient use of exam time.

The best use of exam time was more thoroughly addressed in the second series of simulations. In both the T_1 and T_2 cases (Fig. 4a,b), multiple averaging of dual-angle data provides greater precision per unit scan time than single average, multiple flip angle data. Fitting an exponential curve to the T_1NR values of interest, the effects of both increased flip angles and increased averages are characterized by:

$$T_1NR|_{Nimages}^{Nfa} = T_1NR_{2images} \times (Nimages/2)^{0.44} \quad [17]$$

$$T_1NR|_{Nimages}^{Nav} = T_1NR_{2images} \times (Nimages/2)^{0.5} \quad [18]$$

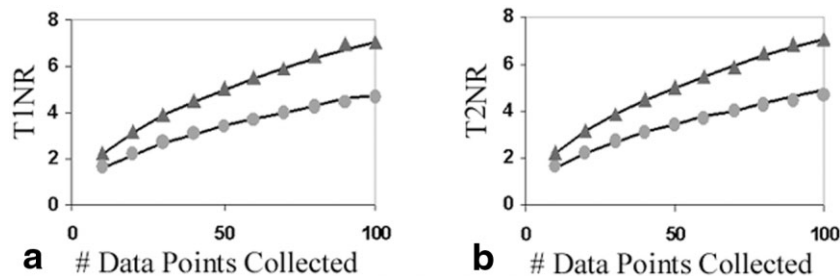
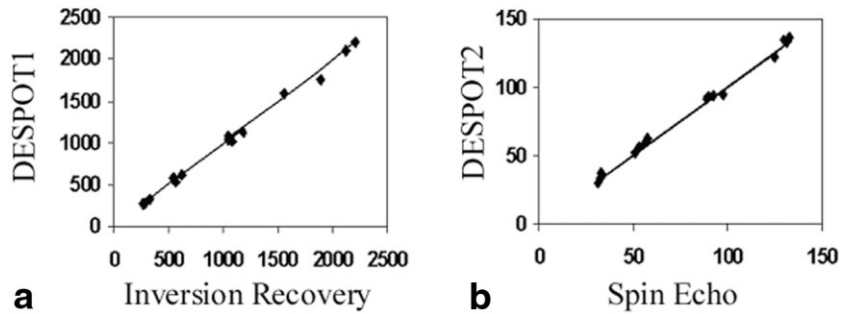


FIG. 4. **a:** Simulated T_1 precision vs. Number of data points collected. **b:** Simulated T_2 precision vs. Number of data points collected. Precision vs. the number of tuned flip angles sampled is shown by the circular points and follows the relationship described by Eqs. [17] and [19]. Precision vs. the number of averages is shown by the triangular points and follows the relationship described by Eqs. [18] and [20]. For both T_1 and T_2 it is clear that averaging produces the greater precision for any number of total images collected.

FIG. 5. **a:** Comparison of T_1 values (ms) calculated from IR data and DESPOT1 data. **b:** Comparison of T_2 values (ms) calculated using SE and DESPOT2 data. In both cases, the points represent average values from a region of interest within each tube of the phantom and the solid line represents the line of unity. Close agreement is observed in both the T_1 and T_2 cases.



where $T_1NR|^{Nfa}$ and $T_1NR|^{Nav}$ are the precision values associated with multiple flip angles and multiple averages, respectively. From these curves, it is clear that for any number of acquisitions averaging the ideal dual-angle data provides greater T_1 precision.

Similarly, T_2NR vs. Nfa and Nav (Fig. 4b) can be modeled with analogous functions:

$$T_2NR|_{Nimages}^{Nfa} = T_2NR_{2images} \times (Nimages/2)^{0.44} \quad [19]$$

$$T_2NR|_{Nimages}^{Nav} = T_2NR_{2images} \times (Nimages/2)^{0.5}. \quad [20]$$

As in the T_1 case, it is clear that increasing the number of averages of the ideal dual-angle data provides better T_2 precision than increasing the number of individual points along the regression line.

The above equations and figures clearly illustrate the advantage of averaging the dual-angle data. However, since we are not limited to either just averaging or sampling individual points, but rather have a variety of possible flip angle and averaging combinations available to us, it is advantageous to derive an expression for any case. Combining Eqs. [17] and [18] and Eqs. [19] and [20] provides the analytical expression for the resulting T_1NR or T_2NR for any arbitrary flip angle and averaging combination:

$$T_{1or2}NR_{Nfa} = T_{1or2}NR_{2images} \times (Nfa/2)^{0.44} \times (Nimages/Nfa)^{0.5}. \quad [21]$$

In an additional simulation that examined T_1NR_{Nfa} for a variety of flip angle and averaging combinations, we confirmed that precision is maximized through averaging. Setting an acquisition limit of 100 in which the data from 2 angles could be averaged 50 times, etc., we calculated

T_1NR and compared the simulation results with our proposed model. The model closely follows the simulation data and confirms that averaging is the most efficient use of exam time.

We also examined the precision in T_2 over a range of T_1 and T_2 values, with and without error included in the T_1 measurement. The results of this simulation reveal the SSFP method has maximum precision in the low-to-mid-range T_1 and T_2 (400–2000 ms and 20–100 ms, respectively), which encompasses most brain tissues (with the exception of CSF). When 10% error is included in the T_1 estimate the average precision across the range of T_1 and T_2 values decreases 6%, but still performs well over low to mid T_1 and T_2 range.

Experimental Results

A summary of the phantom T_1 measurements is shown in Fig. 5a and demonstrates the close agreement between the DESPOT1 and IR values. Analysis of variance (ANOVA) carried out between the sets of data yields a P value of 0.47, confirming that no statistical difference exists between the groups. This agreement is also demonstrated by the low mean percent difference (3.4%) between the groups.

Phantom T_2 measurements are summarized in Fig. 5b. The calculated P value between the DESPOT2 and SE values of 0.49 indicates that the two approaches are equivalent. Once again, the mean percent difference between the groups also demonstrates the close agreement of the two approaches with a 5.6% difference between SE and DESPOT2.

Table 1 contains a summary of brain T_1 and T_2 values along with reference IR, SE, and literature values (23–25). As with the phantom data, strong agreement exists between the DESPOT1 or DESPOT2 values and the reference

Table 1
 T_1 and T_2 Values for Six Common Brain Tissues Calculated Using IR, SE, and SPGR/SSFP With the Ideal Angles

Tissue	T_1		T_2	
	IR	DESPOT1	SE	DESPOT2
Gray matter	1002 [56]	1060 [133]	92.1 [2.6]	97.5 [7.3]
White matter	615 [12]	621 [61]	69.4 [1.5]	58.1 [4.1]
Thalamus	818 [18]	780 [55]	72.7 [1.6]	72.1 [4.3]
Putamen	1054 [27]	1014 [101]	71.6 [1.5]	74.1 [4.6]
Globus pallidus	780 [18]	726 [53]	54.6 [2.2]	54.7 [7.2]
Caudate nucleus	1068 [32]	1112 [132]	79.4 [1.9]	86.7 [6.7]

Average values are given with standard deviations shown in brackets.

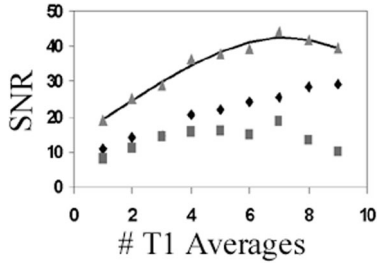


FIG. 6. T_1NR (diamond), T_2NR (square), $T_1NR + T_2NR$ (triangle), and the line fit to $T_1NR + T_2NR$ calculated from various exam time combinations. The total number of images was held constant while the number of T_1 and T_2 images collected was varied. Maximum $T_1NR + T_2NR$ occurred with seven T_1 map averages and three T_2 map averages.

values, with mean absolute differences of: DESPOT1-IR = 7.1%, DESPOT1-literature = 6.4%, DESPOT2-SE = 5.9% and DESPOT2-literature = 10.6%.

Although the precision of the DESPOT1 values is 3 times worse than the precision observed in the IR results, from Eq. [26] we would expect that equivalent precision could be obtained with DESPOT1 by increasing the SNR of the SGPR images by a factor of 3. The resulting scan time of 16 min represents a significant decrease in imaging time compared with the 75 min required by the 8-point IR technique.

The lower precision of the DESPOT2 measurements (compared with SE) could also be remedied with a similar approach resulting in a total DESPOT1 and DESPOT2 experiment time of just 32 min.

Previously, we theoretically predicted that by using a 75:25 split for the $T_1:T_2$ portions of the exam time, maximum $T_1NR + T_2NR$ would be achieved. To experimentally validate this, we performed an experiment in which the $T_1:T_2$ portions of the exam time were divided as follows: 9:1, 8:2, 7:3, 6:4, 5:5, 4:6, 3:7, 2:8, and 1:9. The results of this experiment (Fig. 6) confirm our theoretical prediction. Fitting a polynomial to this curve and solving for the maximum shows the ideal ratio to be 73:27, which closely matches our theoretical prediction.

Reproducibility of the T_1 and T_2 results, determined by calculating the percent SD of a white matter region of interest from four independent experiments, was 6.5% and 5.5% respectively.

Comparison Results

Comparison of the combined DESPOT1 and DESPOT2 approach with conventional and accelerated mapping strategies is summarized in Fig. 7 with representative images shown in Fig. 8. The results of these comparisons reveal that our approach has greater efficiency than alternative mapping methods, with the optimized DESPOT1 and DESPOT2 methods showing relative efficiencies of 3.3 (normalized to 8-point IR) and 2.65 (normalized to 7-point SE), respectively.

Unlike Crawley and Henkelman (22), who first determined the optimum experimental parameters for each sequence (i.e., number of TI data points collected, etc.), in our analysis we simply collected the data in a typical

manner. This may not have optimized the precision achieved or minimized the required scan time for each strategy. Thus, the value of efficiency may be underestimated in some cases. In the case of IR and SR, Crawley and Henkelman showed maximum efficiency is achieved by sampling at just five TI points along the recovery curve. Taking this decrease in imaging time into account increases the efficiency of these methods by 20% and 16%, respectively. However, DESPOT1 would still outperform both methods by factors of 2 and 1.5, respectively.

With the FSE-IR sequence, using an ETL of 4 decreases T_{seq} by a similar factor. Optimistically, assuming T_1NR will not decrease significantly, we would expect this sequence to have a relative efficiency of 2 compared to IR. Experimentally, this parameter was 2.04. While it is reasonable to assume that increasing the ETL to 8 or 16 would further increase the efficiency of this sequence, increases in ETL result in undesirable accuracy decreases due to T_2 decay effects along the echo train.

Likewise, increasing the ETL in the FSE sequence may have further increased its efficiency value. Unfortunately, the signal loss and edge blurring associated with these high ETL values also leads to undesirable decreases in accuracy as well as image degradation.

DESPOT1 and DESPOT2 are also shown to provide superior efficiency compared to the alternative accelerated T_1 mapping strategies of SNAPSHOT FLASH, Look-Locker and accelerated Look-Locker, and T_2 strategies of T_2 FARM and SNAPSHOT FLASH.

DISCUSSION

The experimental and numerical simulation findings presented in the previous sections confirm our hypothesis that the DESPOT1/DESPOT2 approach is an accurate, precise, and high-speed method for combined T_1 and T_2 mapping. The approach permits measurement of T_1 and T_2 in a 3D volume ($256 \times 256 \times 100$) matrix in less than 13 min with less than 7% error in both T_1 and T_2 (compared with reference IR and SE values) for T_1 between 300 and 2000 ms and T_2 between 30 and 150 ms.

While we have presented concise analytical expressions for the ideal SPGR and SSFP angles, they require a priori

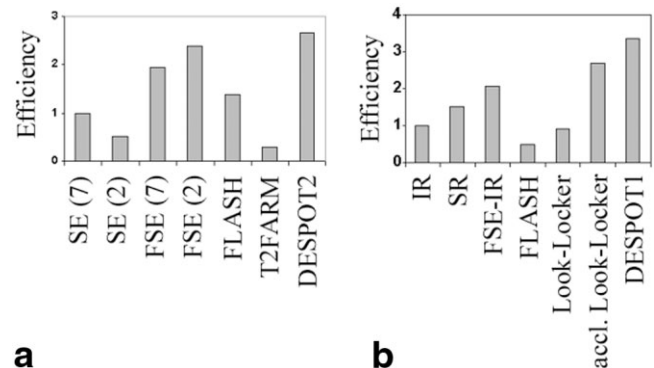


FIG. 7. Bar graphs comparing the relative efficiencies of (a) DESPOT1 and (b) DESPOT2 with alternative T_1 and T_2 mapping methods, respectively.

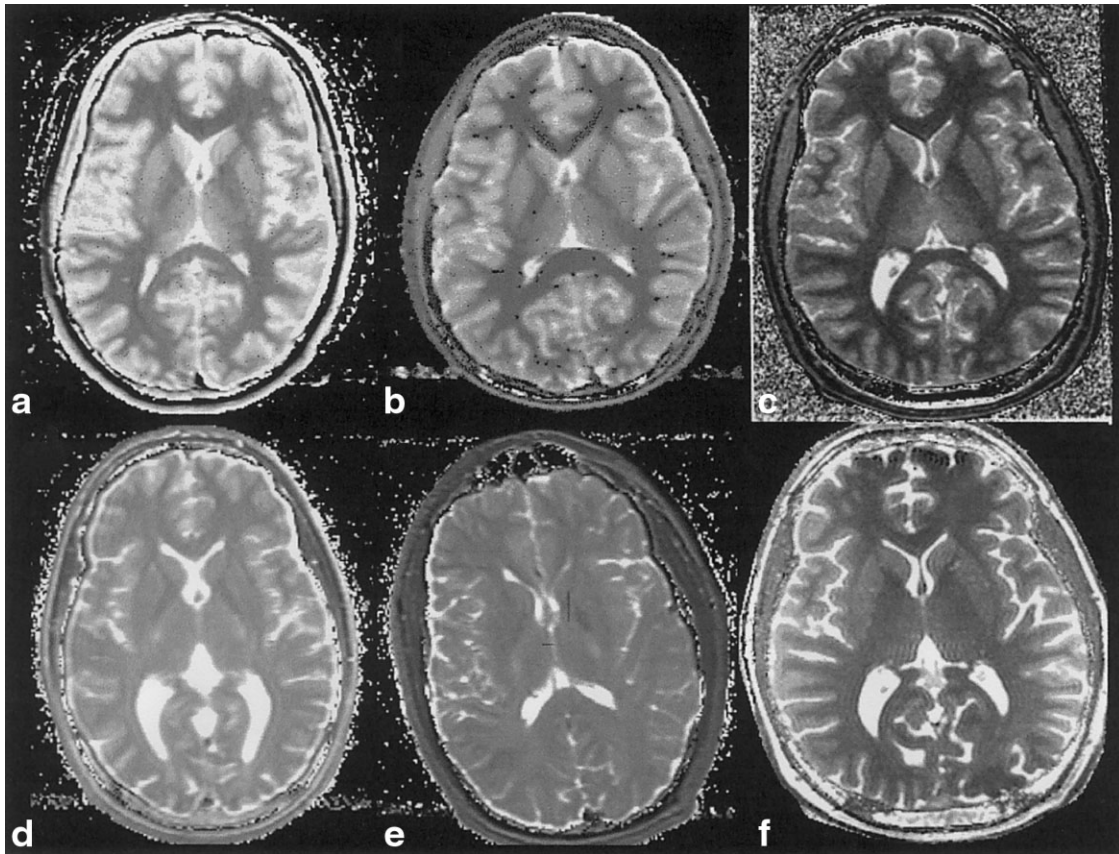


FIG. 8. Axial T_1 and T_2 maps at approximately the same location acquired using (a) IR, (b) FSE-IR, (c) DESPOT1, (d) SE, (e) FSE and (f) DESPOT2 pulse sequences.

knowledge of the T_1 and T_2 ranges present within the imaged object. This does not present a problem in our application, where approximate T_1 and T_2 values for brain tissue are widely available. However, in instances where these values are not known, rough T_1 and T_2 ranges can be calculated from a set of evenly spaced angles with low resolution over a limited volume. The ideal angles can then be calculated from these approximate ranges. The rapid acquisition and calculation time associated with the presented method allows for this two-step approach without requiring excessively long scan times.

The dominant source of error in the accuracy of the DESPOT1 and DESPOT2 T_1 and T_2 estimates is imprecise knowledge of the flip angles used. Errors in the flip angle arise from two main sources: B_1 field inhomogeneities and slice profile errors. The 3D nature of the sequence decreases the magnitude of slice profile errors within the center portion of the 3D slab, particularly when combined with optimized RF pulse designs (e.g., SLR pulses (26)). Unfortunately, errors due to patient-induced B_1 inhomogeneities are more difficult to correct. Variations in B_1 may occur due to either RF coil nonuniformities or RF attenuation and dielectric resonance effects, particularly at very high field. In our neuroimaging application at 1.5 T, this does not appear to present a significant source of error, given the agreement between our results and the literature, especially towards the center of the brain and the basal ganglia — areas associated with absolute changes in T_1 or

T_2 in disease states. In situations where significant B_1 inhomogeneities are expected, quantitative B_1 mapping could be accomplished as a calibration step, which would then allow for correction of the α values in our DESPOT1 and DESPOT2 methods. This, however, would increase scan time. Alternatively, B_1 -insensitive pulses, such as composite pulses or adiabatic fast passage pulses, could be employed. Further work is required to determine the necessity and practicality of these approaches at 1.5 T and higher field strengths.

With several alternative mapping sequences and methods available, the efficiency of each method provides a useful basis for comparison. With an efficiency, relative to IR, of greater than 3, the optimized DESPOT1 method has a higher efficiency than all of the conventional and accelerated T_1 mapping techniques examined. Relative to the 7-point SE method, optimized DESPOT2 has a greater efficiency (by a factor of 2.65); furthermore, this efficiency is higher than any of the accelerated T_2 mapping methods investigated.

Optimized DESPOT1, with its high efficiency and rapid analysis speed, lends itself to a wide range of imaging applications. For example, fat and blood suppression via inversion nulling techniques use approximate T_1 values for fat or blood. Inaccuracy in the estimate of the T_1 value results in suboptimal fat or blood suppression in the final image. Our DESPOT1 method can be used for a fast initial

scan to accurately determine T_1 , thereby improving the performance of these nulling techniques.

The method also provides a simple method for surface coil intensity corrections across an image. Variations in signal intensity across the image, caused by the use of surface coils, will be present in both input images and will therefore be removed by the mapping process. The “flat” T_1 map can then be used to produce images with any desired T_1 weighting. Combined with a “flat” T_2 map, an image with any combination of T_1 and T_2 weighting is also easily produced.

Finally, since the combined DESPOT1 and DESPOT2 method provides three quantitative parameter maps (T_1 , T_2 , and M_o), this method is highly suited to multispectral segmentation schemes (27,28). Additionally, since the T_1 , T_2 , and M_o maps could be calculated in real time at the scanner console, these segmentation/classification schemes could in principle also be performed via the console or in fact in real time during the pulse sequence. This would present radiologists with the ability to analyze and segment data in close to real time, or possibly even adapt pulse sequence changes based on segmentation and classification of tissues/organs during signal acquisition. Although some of these capabilities have been available previously using nonquantitative T_1 - or T_2 -“weighted” images, we expect that their performance will be greatly enhanced when performed using absolute T_1 and T_2 maps.

CONCLUSION

Our approach of combining DESPOT1 and DESPOT2 permits rapid and precise measurement of both T_1 and T_2 within a clinically acceptable period of time (<15 min) for a large volume ($25 \times 25 \times 10$ cm) with high resolution (<1 mm³ voxels). With a mean error of less than 7% in both T_1 and T_2 and a reproducibility of 6.4% and 5.5%, respectively, the method is comparable to the more conventional approaches, all of which require substantially longer scan times. Additionally, postprocessing time is minimal, requiring less than 1 min for both volumes on a 1 GHz PIII PC.

We conclude that the optimized DESPOT1 and DESPOT2 combination approach allows for fully 3D volumetric combined T_1 and T_2 mapping of the brain, in a clinical setting, for the first time and makes the generation of real-time T_1 and T_2 maps a reality.

ACKNOWLEDGMENTS

We thank James Odegaard and Glencora Borradaile for assistance in phantom preparation and data collection.

APPENDIX A

$$S = f \times S_{\alpha E} \quad [A1]$$

$$\frac{\sin(\alpha)}{1 - E_1 \cos(\alpha)} = \frac{f \times \sin(\alpha_E)}{1 - E_1 \cos(\alpha_E)} \quad [A2]$$

making use of the identities:

$$\cos(\alpha_E) = E_1 \quad \text{and} \quad \sin(\alpha_E) = \sqrt{1 - E_1^2}$$

gives:

$$\sin(\alpha)(1 - E_1^2) = f \sqrt{1 - E_1^2} (1 - E_1 \cos(\alpha)) \quad [A3]$$

squaring both sides and expanding:

$$(1 - \cos^2(\alpha))(1 - E_1^2)^2 = f^2(1 - E_1^2)(1 - 2E_1 \cos(\alpha) + E_1^2 \cos^2(\alpha)) \quad [A4]$$

dividing through by and rearranging:

$$(1 - E_1^2) - (1 - E_1^2) \cos^2(\alpha) = f^2 - 2f^2 E_1 \cos(\alpha) \quad [A5]$$

$$0 = f^2 - (1 - E_1^2) - 2f^2 E_1 \cos(\alpha) + (f^2 E_1^2 + 1 - E_1^2) \cos^2(\alpha) \quad [A6]$$

using the quadratic formula:

$$\cos(\alpha) = \frac{f^2 E_1 \pm \sqrt{-f^2(1 - E_1^2)^2 + (1 - E_1^2)^2}}{f^2 E_1^2 + 1 - E_1^2} \quad [A7]$$

therefore:

$$\alpha = \cos^{-2} \left(\frac{f^2 E_1 \pm (1 - E_1^2) \sqrt{1 - f^2}}{1 - E_1^2(1 - f^2)} \right). \quad [A8]$$

APPENDIX B

$$S = f \times S_{\alpha E} \quad [A9]$$

$$\frac{(1 - E_1) \sin(\alpha)}{1 - E_1 E_2 - (E_1 - E_2) \cos(\alpha)} = \frac{f \times (1 - E_1) \sin(\alpha_E)}{1 - E_1 E_2 - (E_1 - E_2) \cos(\alpha_E)} \quad [A10]$$

making use of the identities:

$$\cos(\alpha_E) = \Psi \quad \text{and} \quad \sin(\alpha_E) = \sqrt{(1 - \Psi^2)}$$

where:

$$\Psi = (E_1 - E_2) / (1 - E_1 E_2) \quad [A11]$$

squaring both sides:

$$\sin^2(\alpha)(1 - E_1 E_2 - (E_1 - E_2) \Psi)^2 = f^2(1 - \Psi^2)^2(1 - E_1 E_2 - (E_1 - E_2) \cos(\alpha))^2 \quad [A12]$$

expanding and collecting like terms:

$$\begin{aligned} & \cos^2(\alpha)[2E_1E_2 + E_1E_2\Psi - 2E_1E_2(E_1 - E_2)\Psi + E_1^2E_2^2 \\ & \quad + (E_1 - E_2)^2\Psi^2 - f^2(1 - \Psi)(E_1 - E_2)^2] \\ & + \cos(\alpha)[2f^2(1 - \Psi)(E_1 - E_2) - 2f^2(1 - \Psi)E_1^2(E_1 - E_2)] \\ & \quad + (1 - 2E_1E_2 - 2(E_1 - E_2)\Psi + 2E_1E_2(E_1 - E_2)\Psi \\ & \quad + E_1^2E_2^2 + (E_1 - E_2)^2\Psi^2 - f^2(1 - \Psi) \\ & \quad + 2f^2(1 - \Psi)E_1E_2 - f^2(1 - \Psi)E_1^2E_2^2] = 0. \quad [\text{A13}] \end{aligned}$$

Thus setting:

$$A = 2E_1E_2 + 2E_1E_2\Psi - 2E_1E_2(E_1 - E_2)\Psi + E_1^2E_2^2 \\ + (E_1 - E_2)^2\Psi^2 - f^2(1 - \Psi)(E_1 - E_2)^2 \quad [\text{A14}]$$

$$B = 2f^2(1 - \Psi)(E_1 - E_2) - 2f^2(1 - \Psi)E_1E_2(E_1 - E_2) \quad [\text{A15}]$$

$$C = 1 - 2E_1E_2 - 2(E_1 - E_2)\Psi + 2E_1E_2(E_1 - E_2)\Psi \\ + E_1^2E_2^2 + (E_1 - E_2)^2\Psi^2 - f^2(1 - \Psi) \\ + 2f^2(1 - \Psi)E_1E_2 - f^2(1 - \Psi)E_1^2E_2^2 \quad [\text{A16}]$$

allows for the solution using the quadratic equation:

$$\alpha = \cos^{-1}((-B \pm \sqrt{B^2 - 4AC})/2A). \quad [\text{A17}]$$

APPENDIX C

Following the laws for propagation of error, we are able to examine the impact of error in the measured DESPOT1 signal intensities on the T_1 estimate. Starting from Eq. [3a] we obtain an expression for the error in the T_1 (dT_1) as:

$$\frac{\delta T_1}{T_1} = \frac{\delta m}{m} \times \frac{1}{\ln(m)} \quad [\text{A18}]$$

assuming we use the ideal angles where $S_{\alpha_1} = S_{\alpha_2} = S$:

$$\frac{\delta T_1}{T_1} = \frac{\delta S}{S} \times \sqrt{\frac{\tan^2\alpha_1 + \tan^2\alpha_2 - 0.5 \tan\alpha_1 \tan\alpha_2}{\tan^2\alpha_1 + \tan^2\alpha_2}} \times \frac{1}{\ln(m)} \quad [\text{A19}]$$

$$\frac{\delta T_1}{T_1} = \frac{\delta S}{S} \times \frac{1}{G_1}. \quad [\text{A20}]$$

Rewriting Eq. [A20] in terms of image SNR and introducing the new term T_1NR (T_1 -to-Noise Ratio), which provides a measure of the T_1 precision as the average T_1 divided by the standard deviation, we obtain the final expression:

$$T_1NR = SNR \times G_1. \quad [\text{A21}]$$

In a similar manner, we can determine the uncertainty in T_2 . Starting with Eq. [6a] and letting:

$$a = (m - E_1)/(mE_1 - 1) \quad [\text{A22}]$$

and assuming we use the ideal angles where $S_{\alpha_1} = S_{\alpha_2} = S$, we obtain the expression:

$$\frac{\delta T_2}{T_2} = \sqrt{\frac{\delta S^2}{S^2} (A + B) + \delta T_1^2(C + D)} \times \frac{1}{\ln(a)} \quad [\text{A23}]$$

with:

$$A = \frac{m^2}{(m - E_1)^2} \left(\frac{\tan^2\alpha_1 + \tan^2\alpha_2 - 0.5 \tan\alpha_1 \tan\alpha_2}{\tan^2\alpha_1 + \tan^2\alpha_2} \right. \\ \left. + \frac{\sin^2\alpha_1 + \sin^2\alpha_2 - 0.5 \sin\alpha_1 \sin\alpha_2}{\sin^2\alpha_1 + \sin^2\alpha_2} \right) \quad [\text{A24a}]$$

$$B = (E_1^2 \times TR^2)/(T_1^4 \times (m - E_1)^2). \quad [\text{A24b}]$$

$$C = \frac{m^2 E_1^2}{(mE_1 - 1)^2} \left(\frac{\tan^2\alpha_1 + \tan^2\alpha_2 - 0.5 \tan\alpha_1 \tan\alpha_2}{\tan^2\alpha_1 + \tan^2\alpha_2} \right. \\ \left. + \frac{\sin^2\alpha_1 + \sin^2\alpha_2 - 0.5 \sin\alpha_1 \sin\alpha_2}{\sin^2\alpha_1 + \sin^2\alpha_2} \right) \quad [\text{A24c}]$$

$$D = (m^2 \times E_1^2 \times TR^2)/(T_1^4 \times (mE_1 - 1)^2). \quad [\text{A24d}]$$

When T_1 is large (>100 ms), $C+D \approx 0$, so we can simplify Eq. [A23] to:

$$\frac{\delta T_2}{T_2} = \frac{\delta S}{S} \times \frac{1}{G_2}, \quad [\text{A25}]$$

which we can rewrite in terms of image SNR and T_2NR (T_2 -to-Noise Ratio) as:

$$T_2NR = SNR \times G_2. \quad [\text{A26}]$$

REFERENCES

1. Detre JA, Leigh JS, Williams DS, Koretsky AP. Perfusion imaging. *Magn Reson Med* 1992;23:37–45.
2. Gowland P, Mansfield P, Bullock P, Stehling M, Worthington B, Firth J. Dynamic studies of gadolinium uptakes in brain tumours using inversion recovery echo-planar imaging. *Magn Reson Med* 1992;26:241–258.
3. Pitkamen A, Laakso M, Kalviainen R, Partanen K, Vainio P, Lehtovirta M, Riekinen P, Soininen H. Severity of hippocampal atrophy correlates with the prolongation of MRI T_2 relaxation time in temporal lobe epilepsy but not in Alzheimer's disease. *Neurology* 1996;46:172–1730.
4. Vymazal J, Righini A, Brooks RA, Canesi M, Mariani C, Leonardi M, Pezzoli G. T_1 and T_2 in the brain of healthy subjects, patients with Parkinson's disease, and patients with multiple system atrophy: relation to iron content. *Radiology* 1999;211:489–495.
5. Bluml S, Schad LR, Boris S, Lorenz WJ. Spin-lattice relaxation time measurement by means of a TurboFLASH technique. *Magn Reson Med* 1993;30:289–295.
6. Brix G, Schad LR, Deimling M, Lorenz WJ. Fast and precise T_1 imaging using a TOMROP sequence. *Magn Reson Imag* 1990;8:351–356.
7. Henderson E, McKinnon G, Lee TY, Rutt BK. A fast 3D Look-Locker method for volumetric T_1 mapping. *Magn Reson Imag* 1999;17:1163–1171.

8. McKenzie CA, Chen Z, Drost DJ, Prato FS. Fast acquisition of quantitative T_2 Maps. *Magn Reson Med* 1999;41:208–212.
9. Deichmann R, Adolf H, Noth U, Morrissey S, Schwarzbauer C, Haase A. Fast T_2 -mapping with SNAPSHOT FLASH imaging. *Magn Reson Imag* 1995;13:633–639.
10. Christensen KA, Grand DM, Schulman EM, Walling C. Optimal determination of relaxation times of Fourier transform nuclear magnetic resonance. Determination of spin-lattice relaxation times in chemically polarized species. *J Phys Chem* 1974;78:1971–1977.
11. Homer J, Beevers MS. Driven-equilibrium single-pulse observation of T_1 relaxation. A re-evaluation of a rapid 'new' method for determining NMR spin-lattice relaxation times. *J Magn Reson* 1985;63:287–297.
12. Homer J, Roberts JK. Conditions for the driven equilibrium single pulse observation of spin-lattice relaxation times. *J Magn Reson* 1987;74:424–432.
13. Wang HZ, Riederer SJ, Lee JN. Optimizing the precision in T_1 relaxation estimation using limited flip angles. *Magn Reson Med* 1987;5:399–416.
14. Homer J, Roberts JK. Routine evaluation of M_0 ratios and T_1 values from driven equilibrium NMR spectra. *J Magn Reson* 1990;87:265–272.
15. Carr HY. Steady-state free precession in nuclear magnetic resonance. *Phys Rev* 1958;112:1693–1701.
16. Hinshaw WS. Image formation by nuclear magnetic resonance: the sensitive-point method. *J Appl Phys* 1976;47:3709–3721.
17. Young IR, Burl M, Bydder GM. Comparative efficiency of different pulse sequences in MR imaging. *J Comput Assist Tomogr* 1986;10:271–285.
18. Perkins TG, Wehrli FW. CSF signal enhancement in short TR gradient echo images. *Magn Reson Imag* 1986;4:465–467.
19. Hendrick RE, Kneeland JB, Stark DD. Maximizing signal-to-noise and contrast-to-noise ratios in FLASH imaging. *Magn Reson Imag* 1987;5:117–127.
20. Hawkes RC, Patx S. Rapid Fourier imaging using steady-state free precession. *Magn Reson Med* 1987;4:9–23.
21. Buxton RB, Fisel CR, Chien D, Brady TJ. Signal intensity in fast NMR imaging with short repetition times. *J Magn Reson* 1989;83:576–585.
22. Crawley AP, Henkelman RM. A comparison of one shot and recovery. Methods in T_1 imaging. *Magn Reson Med* 1988;7:23–34.
23. Vymazal J, Righini A, Brooks RA, Canesi M, Mariani C, Leonardi M, Pezzoli G. T_1 and T_2 in the brain of healthy subjects, patients with Parkinson disease, and patients with multiple system atrophy: relation to iron content. *Radiology* 1999;211:489–495.
24. Breger RK, Rimm AA, Fisher ME, Papke RA, Houghton VM. T_1 and T_2 measurements on a 1.5 T commercial MR imager. *Radiology* 1989;171:283–276.
25. Steen RG, Gronemeyer SA, Kingsley PB, Reddick WE, Langston JS, Taylor JS. Precise and accurate measurement of proton T_1 in human brain in vivo: validation and preliminary clinical application. *J Magn Reson Imag* 1994;4:681–694.
26. Pauly P, Le Roux P, Nishimura D, Macovski A. Parameter relations for the Shinnar–Le Roux selective excitation pulse design algorithm. *IEEE Trans Med Imag* 1991;10:53–65.
27. Mitchell JR, Rutt BK. Improved contrast in multi-spectral phase images derived from MR exams of MS patients. *Med Phys* 2002;29:727–725.
28. Deoni SCL, Rutt BK, Peters TM. An alternative method for visualizing m-dimensional MRI data. In: *Proc 9th Annual Meeting ISMRM, Glasgow, 2001*. p 784.